Full-Scale Tests of Slender Concrete-Filled Tubes: Interaction Behavior

Tiziano Perea, Ph.D., A.M.ASCE[1]; Roberto T. Leon, Ph.D., P.E., F.ASCE[2]; Jerome F. Hajjar, Ph.D., P.E., F.ASCE[3]; and Mark D. Denavit, Ph.D., A.M.ASCE[4]

Abstract: This paper presents selected results from an experimental and computational evaluation on the behavior of slender concrete-filled steel tubes (CFTs) under combined axial compression and biaxial flexure. A complex loading protocol was used in the experimental program, including monotonic and cyclic loading that allowed detailed evaluation of the complete beam-column response. This paper principally addresses the experimental determination of the maximum stable axial load–bending moment ($P-M$) interaction strength. The experimental $P-M$ interaction strengths extracted at incipient instability shows that for very slender specimens, the bilinear interaction diagram proposed in the current design provisions of the AISC is somewhat unconservative. This experimental observation is also confirmed by detailed computational results. However, the results also indicate that current AISC provisions provide an accurate and conservative approach for evaluating axial load–flexural interaction for most practical CFT column sizes and lengths (i.e., composite beam columns with low and intermediate slenderness). **DOI: 10.1061/(ASCE)ST.1943-541X.0000949.**

Author keywords: Full-scale tests; Slender columns; Concrete-filled tubes; Interaction diagram; Beam-column; Composite construction; Composite columns; Metal and composite structures.

Introduction

Composite steel-concrete structural systems constitute a valuable and growing sector of the construction market, often being adopted for some of the more challenging structural configurations because of the high strength and stiffness offered by these systems. Composite columns in the form of either steel-reinforced concrete (SRC) or concrete-filled steel tube (CFT) beam columns have been adopted extensively for tall buildings in Asia in areas of large seismic and wind exposures and are being used increasingly in the United States and Europe for structures of all heights. Previous experimental and analytical work has shown that well-designed concrete-filled tubes have superior stiffness, strength, ductility, and deformation characteristics as compared to structural steel or reinforced concrete beam columns, particularly under cyclic loads (Hajjar 2000; Tort and Hajjar 2003; Leon et al. 2007; Leon and Hajjar 2008; Gourley et al. 2008). However, there are at least three areas where information is needed for composite beam-column elements: (1) the validity of current specifications to estimate the strength of slender composite beam columns, as little data are available for that type of system; (2) the establishment of accurate member flexural stiffness values under cyclic loads for systems incorporating composite beam-column elements; and (3) the development of system behavior factors for composite systems under seismic loads, as current specifications rely solely on similarities to either structural steel or reinforced concrete structural systems to establish these factors.

To address these issues, a multiinstitution-combined experimental and computational research program was undertaken, including: (1) experiments on 18 slender, full-scale concrete-filled steel tube beam columns with the highest hollow structural section (HSS) width-thickness ratios commercially available (Perea et al. 2010; Perea 2010); (2) development of new finite element formulations that enable accurate representation of the seismic response of three-dimensional composite frame structures (Denavit et al. 2010; Denavit 2012); and (3) development of design recommendations for composite structures within the context of specification for structural steel buildings (AISC 2010b).

Perea et al. (2013a) described the axial load behavior in detail, with particular emphasis on the buckling strength of slender members and the determination of the effective stiffness of the members to assess buckling strength. The rest of the research focuses on axial–flexure interaction and has two broad objectives, one at the member/design level and one at the analysis/system level. The first objective at the member/design level is to compare the experimental results to the existing AISC specification (AISC 2010b) cross-section strength-based provisions for slender composite CFTs. Although the tests are cyclic in nature, the relatively low rates of degradation observed during the first two sets of loads applied [load case 1 (LC1) and LC2, described in the preceding sections) mean that the strength obtained from these tests can be taken as an approximate lower bound to the strength that would have been obtained from monotonic tests. The second objective at the analysis/system level is to provide complex experimental data of CFT beam-column behavior that can be used to calibrate and validate advanced analytical models. These models, in turn, will be used to conduct FEMA P695 (FEMA 2009) analyses to validate system factors (ductility, overstrength, and deflection amplification) for structural systems using composite columns (Denavit 2012).

[1]Associate Professor, Departamento de Materiales, Universidad Autónoma Metropolitana, Mexico City 02200, Mexico (corresponding author). E-mail: tperea@azc.uam.mx

[2]Professor and Chair, Dept. of Civil and Environmental Engineering, Virginia Tech, Blacksburg, VA 24061.

[3]Professor and Chair, Dept. of Civil and Environmental Engineering, Northeastern Univ., Boston, MA 02115.

[4]Design Engineer, Stanley D. Lindsey and Associates, 2300 Windy Ridge Parkway SE, Suite 200S, Atlanta, GA 30339.

Note. This manuscript was submitted on February 4, 2013; approved on September 16, 2013; published online on April 22, 2014. Discussion period open until September 22, 2014; separate discussions must be submitted for individual papers. This paper is part of the ***Journal of Structural Engineering***, © ASCE, ISSN 0733-9445/04014054(12)/$25.00.

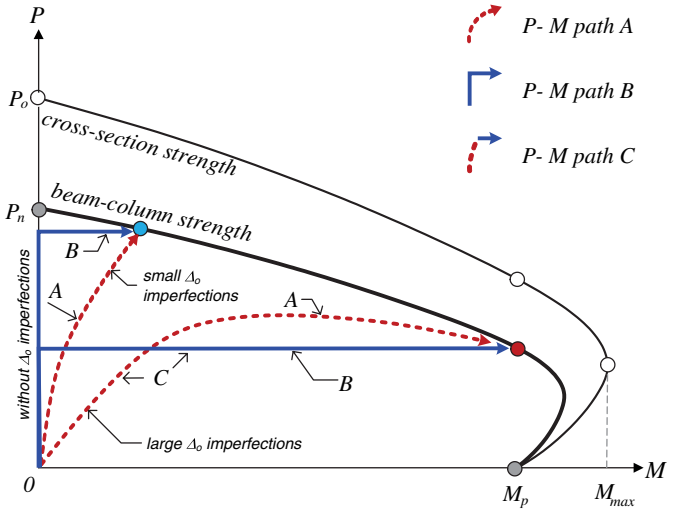

Fig. 1. $P-M$ paths to approach the beam-column capacity

This paper addresses only the comparison to AISC beam-column strength and is intended to complement the column (or axial) strength data described in a previous paper (Perea et al. 2013a). The authors recognize the limits of using data derived from specimens that have been subjected to severe displacement histories in this context but believe that the careful and redundant measurements made has allowed them to properly process the data and minimize errors (Perea et al. 2013b). In the end, both the experimental and analytical results need to be recognized as only approximations to the real values.

Background

Extensive literature exists on the behavior of composite CFT beam columns, including their behavior under large cyclic deformations. Most of the prior work on cyclic performance of composite beam columns was carried out in Japan, Europe, Australia, and the United States, and comprehensive summaries can be found in Kawaguchi et al. (1998), Nishiyama et al. (2002), Roik and Bergmann (1989), Sulyok and Galambos (1995), Lundberg and Galambos (1996), and Gourley et al. (2008). Much of the available experimental data indicate outstanding hysteretic behavior, thus making CFTs suitable for design in high seismic zones. However, many of the prior cyclic tests have been conducted either on relatively stocky specimens, both in terms of flexural and local buckling criteria or without the required test controls and instrumentation to assess cyclic interaction of axial load and biaxial bending moment ($P-M$) behavior in detail.

Determination of $P-M$ Interaction Diagrams

Methods for determining the interaction strength at the cross-section level are well established. Commonly, it can be determined experimentally as the peak strength from tests on stocky members where the geometric nonlinear effects are negligible. In design, a common approach to assess cross-section strength is the strain compatibility method (AISC 2010b; ACI 2011). In this approach, a linear distribution of strain within the cross-section is assumed, stresses are determined through appropriate constitutive relations, and the axial load and bending moment are computed by integration over the cross-section. Concrete cracking and crushing and steel yielding are typically included in the constitutive relations, and additional effects such as concrete confinement, steel local buckling, and strain hardening can be included as well (Sakino et al. 2004; Varma 2000; Denavit and Hajjar 2010; Denavit 2012).

The interaction strength at the beam-column level is more complex, depending on cross-section stiffness and strength as well as member length, end restraint, and initial geometric imperfections. Additionally, different measures for bending moment that are of interest for assessing different performance metrics (e.g., first order versus second order) arise.

In the design of composite members, depending on the strategy used by the provisions to account for beam-column stability, the beam-column interaction strength is often taken as the cross-section interaction strength (ACI 2011) or an interaction surface that reduces the cross-section strength to account for member stability (Leon et al. 2007; AISC 2010b). However, design interaction curves only define the available strength and are intended to be paired with specific analysis procedures. These procedures include the effective length and direct analysis methods (Hajjar et al. 1997;

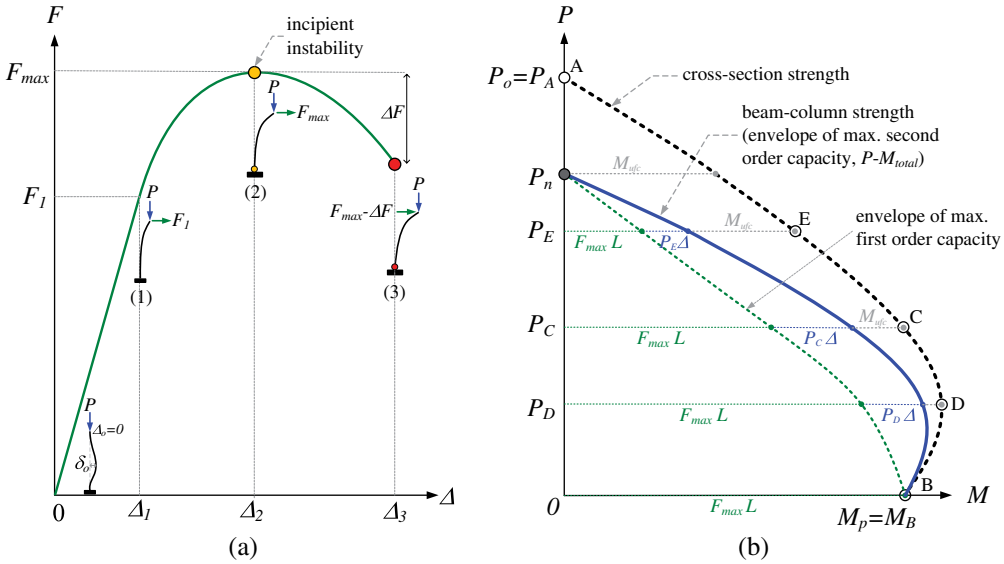

Fig. 2. Determination of the beam-column strength: (a) lateral force—lateral displacement ($F-\Delta$) curve; (b) $P-M$ interaction diagrams

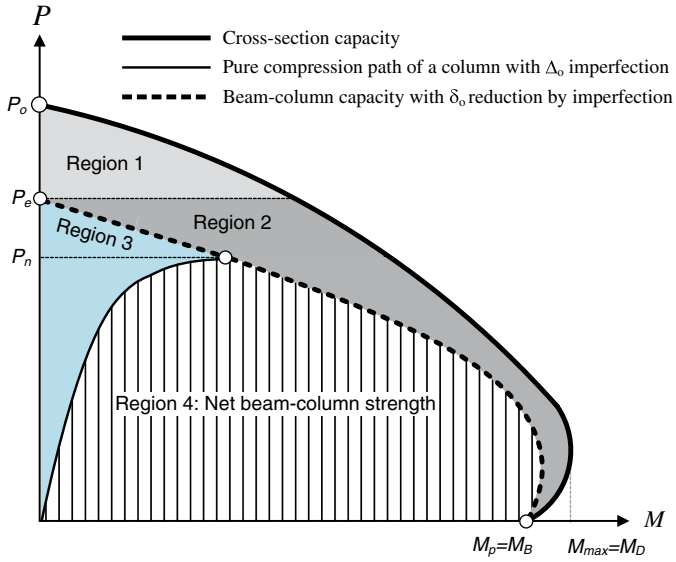

Fig. 3. Components of the $P-M$ interaction diagram for composite members

Surovek-Maleck and White 2004; AISC 2010b), which prescribe equivalent rigidities, initial imperfections, and other conditions to be considered in assessing the required strength. For this reason, under a given set of applied loads, the second-order internal forces will differ between experimental values and those obtained from the elastic analyses used in design. Because of this, experimental strengths are not directly comparable because the interaction diagram is meant to be compared against internal forces from an elastic analysis; however, these two quantities are near enough that their comparison is insightful.

The maximum interaction strength of a beam column may be reached in an experiment or analysis by increasing both the axial and flexural loads proportionally (as in Path A in Fig. 1), increasing one component nonproportionally while holding the second one constant (as in Path B), or a combination (as in Path C) until an unstable condition arises (e.g., an abrupt displacement or failure if the specimen is held in load control). These methods are common in computational studies and are also possible in experimental studies because of the unique control capabilities of the multi-axial subassemblage testing (MAST) facility (Hajjar et al. 2002; French et al. 2004) of the network for earthquake engineering simulation (NEES).

In this research, the method labeled Path B in Fig. 1 was utilized to determine points on the beam-column interaction surface by probes of increasing moment at a constant axial load. Path B is a mixed load-displacement control sequence where an incremental axial load is applied while holding the lateral top displacements to zero, and then lateral displacements are imposed while holding the axial load constant.

This method is schematically illustrated in Fig. 2(a) for the case of a fixed-free ($K = 2.0$) cantilever column with a given length, L (a "Notation" section is included at the end of the paper defining all symbols). First, with no axial load, the column was plumbed by moving the crosshead connected to the column top and so reducing the initial out-of-plumbness, Δ_o, to zero. Then, while holding the column plumbed, a compressive axial load, P, was applied concentrically and held constant at the target value; at this point, the plumbed column with only initial out-of-straightness imperfection, δ_o, is at the origin of the graph in Fig. 2(a). By controlling the lateral displacements at the top of the column, the specimen is then subjected to a monotonically increasing lateral load, F, which is initially resisted elastically (assuming the axial load has not already initiated material inelasticity). Under this loading condition, the maximum total bending moment developed occurs at the column base and is equal to the sum of the overturning or first-order moment, FL, and the second-order effects, $P\Delta$. As the uniaxial lateral top displacement increases beyond Δ_1, the materials begin to behave nonlinearly at the base as the concrete cracks and crushes and the steel yields and strain hardens as a plastic hinge forms at that location. At some displacement, Δ_2, the beam column reaches incipient instability as indicated by an inability to carry additional lateral load. At this peak lateral load, $F_{\max}$, the cross-section may not be fully plasticized, and there may be some remaining flexural strength at the cross-section level. Loading can continue if the column is held in its unstable configuration, as was done in the experiments through displacement control of the actuators that imposed the lateral load. As the lateral displacement is increased

Table 1. Test Matrix with Measured Values

Specimen name	L (m)	HSS section	F_y (MPa)	F_u (MPa)	E_s (GPa)	f'_c (MPa)	f_c (MPa)	f_t (MPa)	E_c (GPa)	λ
1-C5-18-5	5.50	141.3 × 3.4	383	487	194.0	37.9	37.9	7.6	27.6	0.90
2-C12-18-5	5.50	323.9 × 6.4	337	446	199.2	37.9	38.6	7.6	27.6	1.55
3-C20-18-5	5.52	508.0 × 6.4	328	471	200.3	37.9	40.0	7.6	27.6	1.05
4-Rw-18-5	5.54	508 × 305 × 7.9	365	502	202.4	37.9	40.7	7.6	27.6	1.38
5-Rs-18-5	5.54	508 × 305 × 7.9	365	502	202.4	37.9	40.7	7.6	27.6	0.88
6-C12-18-12	5.50	323.9 × 6.4	337	446	199.2	87.6	91.0	11.4	41.9	1.90
7-C20-18-12	5.53	508.0 × 6.4	328	471	200.3	87.6	91.0	11.4	41.9	1.30
8-Rw-18-12	5.55	508 × 305 × 7.9	365	502	202.4	87.6	91.7	11.4	41.9	1.65
9-Rs-18-12	5.55	508 × 305 × 7.9	365	502	202.4	87.6	91.7	11.4	41.9	1.04
10-C12-26-5	7.95	323.9 × 6.4	335	470	200.2	50.3	54.5	4.1	34.5	2.38
11-C20-26-5	7.99	508.0 × 6.4	305	477	201.7	50.3	55.8	4.1	34.5	1.61
12-Rw-26-5	7.96	508 × 305 × 7.9	406	534	200.1	50.3	56.5	4.1	34.5	2.14
13-Rs-26-5	7.97	508 × 305 × 7.9	383	505	200.2	50.3	57.2	4.1	34.5	1.35
14-C12-26-12	7.96	323.9 × 6.4	383	461	198.3	79.3	80.0	5.2	40.0	2.72
15-C20-26-12	7.98	508.0 × 6.4	293	454	200.1	79.3	80.0	5.2	40.0	1.78
16-Rw-26-12	7.96	508 × 305 × 7.9	381	506	200.5	79.3	80.7	5.2	40.0	2.30
17-Rs-26-12	7.96	508 × 305 × 7.9	380	496	200.1	79.3	80.7	5.2	40.0	1.46
18-C5-26-12	7.94	141.3 × 3.4	383	487	194.0	79.3	80.7	5.2	40.0	1.51

Note: F_y, F_u, and E_s = yielding stress, ultimate stress, and Young's modulus of the HSS steel section, respectively; f'_c and f_c = compression concrete strength at the 28th day and at the testing day, respectively; f_t and E_c = tension strength and the Young's modulus of the concrete, respectively; L = column length; λ = slenderness parameter calculated as defined by AISC (2010b).

Table 2. Description of Loading Cases: Uniaxial Flexure (LC2) and Biaxial Flexure (LC3)

	LC2—unidirectional				LC3—bidirectional			
Specimen	K	P (kN)	Direction	Reversal	K	P (kN)	Shape	Reversal
1-C5-18-5	2	66.7	Principal x-axis	F_{max}	—	—	—	—
		133.4				—	—	—
2-C12-18-5	2	1,334.5	Principal x-axis	F_{max}	2	1,112.1	Fig. 4(a)	F_{max}/probe
		889.6				667.2	8 probes	X or Y
		444.8				—	—	—
3-C20-18-5	2	4,448.2	Imperfection	F_{max}	2	5,560.3	Fig. 4(a)	F_{max}/probe
		2,224.1				3,336.2	16 probes	X or Y
		—				1,112.1	—	—
4-Rw-18-5	2	2,668.9	Principal x-axis	F_{max}	2	3,336.2	Fig. 4(a)	F_{max}/probe
		1,334.5				2,001.7	8 probes	X or Y
		—				667.2	—	—
5-Rs-18-5	2	4,448.2	Principal x-axis	F_{max}	2	3,336.2	Fig. 4(a)	F_{max}/probe X or Y
		2,224.1				1,112.1	8 probes	—
6-C12-18-12	2	1,334.5	Imperfection	F_{max}	2	1,668.1	Fig. 4(a)	F_{max}/probe
		667.2				1,000.8	8 probes	X or Y
		—				333.6	—	—
7-C20-18-12	2	4,448.2	Imperfection	F_{max}	2	5,560.3	Fig. 4(a)	F_{max}/probe
		2,224.1					8 probes	X or Y
8-Rw-18-12	2	2,668.9	Principal x-axis	F_{max}	2	3,558.6	Fig. 4(a)	F_{max}/probe
		1,334.5				—	8 probes	X or Y
9-Rs-18-12	2	5,337.9	Principal x-axis	F_{max}	2	3,558.6	Fig. 4(b)	F_{max}/probe
		1,779.3				—	6 main probes with subprobes each	X or Y
10-C12-26-5	2	889.6	Imperfection	Δ—targets 1% increments	2	667.2	Fig. 4(c)	Δ—targets 1% increments
		444.8				222.4	—	—
11-C20-26-5	2	2,668.9	Imperfection	Δ—targets 1% increments	2	2,001.7	Fig. 4(c)	Δ—targets 1% increments
		1,334.5				667.2	—	—
12-Rw-26-5	2	1,779.3	Principal x-axis	Δ—targets 1% increments	2	1,334.5	Fig. 4(c)	Δ—targets 1% increments
		889.6				2,224.1	—	—
13-Rs-26-5	2	1,779.3	Principal x-axis	Δ—targets 1% increments	2	1,334.5	Fig. 4(c)	Δ—targets 1% increments
		3,558.6				2,224.1	—	—
14-C12-26-12	2	444.8	Imperfection	Δ—targets 1% increments	2	667.2	Fig. 4(c)	Δ—targets 1% increments
		889.6				—	—	—
	1	1,334.5	Imperfection	Δ—targets 1% increments	1	1,334.5	Fig. 4(c)	Δ—targets 1% increments
		2,001.7				—	—	—
15-C20-26-12	2	1,779.3	Imperfection	Δ—targets 1% increments	2	889.6	Fig. 4(c)	Δ—targets 1% increments
		3,558.6				2,668.9	—	—
16-Rw-26-12	2	889.6	Principal x-axis	Δ—targets 1% increments	2	1,334.5	Fig. 4(c)	Δ—targets 1% increments
		1,779.3				2,224.1	—	—
17-Rs-26-12	2	1,779.3	Principal x-axis	Δ—targets 1% increments	2	889.6	Fig. 4(c)	Δ—targets 1% increments
		3,558.6				2,668.9	—	—
18-C5-26-12	1	66.7	Imperfection	Δ—targets 1% increments	1	89.0	Fig. 4(c)	Δ—targets 1% increments
		111.2				—	—	—

and the second-order effects become more dominant, a reduction in the lateral load and increase in the moment at the base are observed. Eventually, at displacement Δ_3, the cross-section strength will be reached, and the moment at the base will cease to rise.

The peak second-order moment at incipient buckling is termed the maximum safe second-order moment, M_{total}; the increase in moment from the point of incipient buckling to the point where the cross-section strength is reached is termed the unusable flexural strength, M_{ufc}. The sum of these two components equals the cross-section strength moment for a given level of axial force. The interaction diagram is then defined by repeating this process on the same beam column, determining the M_{total} for different values of sustained axial load, P, as shown in Fig. 2(b) (curve with the label *beam-column strength*). The axial load levels used in the loading protocol were often applied between the anchor points C_λ and D_λ as defined by AISC (2010b), i.e., a zone in which the flexural strength in composite sections is equal or larger than the flexural strength in pure bending. The first sets of interaction $P-M_{total}$ values obtained with the mentioned approach are assumed to be the full expected strength for the composite beam column; however, as the damage accumulates during an experimental test, evidenced by steel local buckling and concrete crushing at the column base, the available total flexural strength (M_{total}) of the composite member is expected to decrease.

Also of interest on the total $P-M$ diagram are the components for the first-order moment and the additional $P\Delta$ moment, which are indicative of the maximum external load that can be applied and the effects of geometric nonlinearity, respectively. The first-order moments are equal to the second-order moments in two cases: the first is at the pure flexural strength, M_p, where the absence of axial load precludes any second-order effects; the second is at the pure compression strength, P_n, where the absence of lateral deflection precludes any second-order effects.

The total $P-M$ diagram of the beam column, obtained as described previously and shown in Fig. 2(b), has no consideration of the initial out-of-plumbness, Δ_o, because this was removed at the beginning of the load case [as schematically illustrated at the original point of Fig. 2(a)]. However, the initial imperfections must be

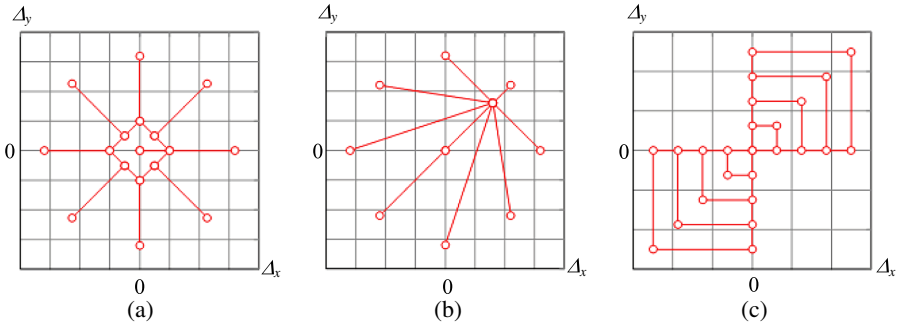

Fig. 4. Horizontal displacement path at the top during LC3: (a) biaxial 8 probes, Specimens 2 to 7; (b) biaxial probe with subprobes, Specimen 9; (c) incremental biaxial (eight), Specimens 8 and 10 to 18

considered in design to account for the erection tolerances by the standards [ASTM A6/A6M (ASTM 2013); AISC 2010a].

Two alternatives to account for the initial out-of-plumbness, Δ_o, in strength design are:

- Accounting for the initial out-of-plumbness, Δ_o, in the required strength by consideration of these imperfections in the second-order analysis through either directly modeling the initial out-of-plumbness or by adding appropriate notional loads. This is consistent with the requirements of the direct analysis method (DAM) and effective length method in the AISC specification (AISC 2010b).
- Accounting for the initial out-of-plumbness, Δ_o, in the available strength by utilizing a design interaction surface based on the net moment, M_{net}. The net moment is equal to the total second-order moment, M_{total}, minus the second-order moment caused by the initial out-of-plumbness (Region 3 in Fig. 3). An attractive feature of interaction diagrams constructed with M_{net} is that the pure axial strength corresponds to that of a geometrically imperfect column (affected both by δ_o and Δ_o). This is useful when the moments caused by the initial imperfections are not captured in the analysis to determine required strength.

Fig. 3 shows the net $P-M$ beam-column strength (Region 4) as the cross-section $P-M$ strength reduced by instability because of axial compression (Region 1), the unusable flexural strength (Region 2), and the strength consumed by the initial out-of-plumbness imperfection (Region 3). In contrast, the total $P-M$ diagram is the cross-section $P-M$ strength reduced only by instability because of axial compression (Region 1) and the unusable flexural strength (Region 2).

The net moment depends on the magnitude of the geometric imperfections. Because the measured imperfections in many specimens of the experimental program (Perea et al. 2013a) were larger than those permitted by standards [ASTM A6/A6M (ASTM 2013); AISC 2010a), the experimental net moment strengths will be lower than those expected of columns within the standard tolerances.

Experimental Tests

In this test series, 18 specimens with different steel-tube shapes, high width-to-thickness ratios, large slenderness for flexural buckling, and both normal- and high-strength concrete were tested (Table 1). The tests were labeled by a test number–shape–length–concrete strength convention (Perea 2010; Perea et al. 2013a); thus, Specimen 8-Rw-18-12 corresponds to the eighth specimen in the series, with a rectangular cross-section loaded along its weak axis (C# was used for circular sections, where "#" indicates the tube diameter), with a length of 5.5 m (18 ft), and a nominal concrete strength of 83 MPa (12 ksi). The specimens were tested at the NEES MAST facility, a large universal testing machine with precise six degrees of freedom (DOF) control of both load (forces and moments) and deformations (displacements and rotations) at the top crosshead (Hajjar et al. 2002; French et al. 2004). The 18 specimens were initially subjected to a series of buckling tests under a test protocol labeled LC1, whose results are described in Perea et al. (2013a). Following application of LC1, the specimens were tested as beam columns subjected to load cases LC2 and LC3. The first cycles of both LC2 (uniaxial) and LC3 (biaxial) were

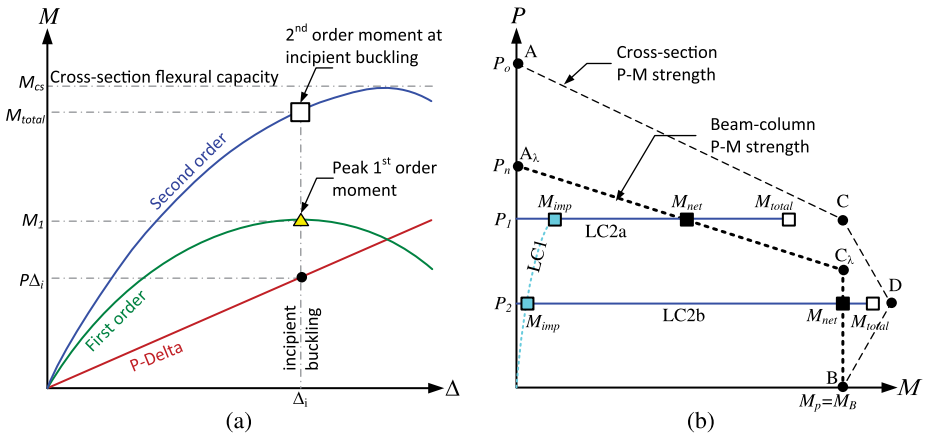

Fig. 5. Schematic illustration of the extraction of $P-M$ interaction points: (a) incipient buckling definition; (b) $P-M$ points from uniaxial loading

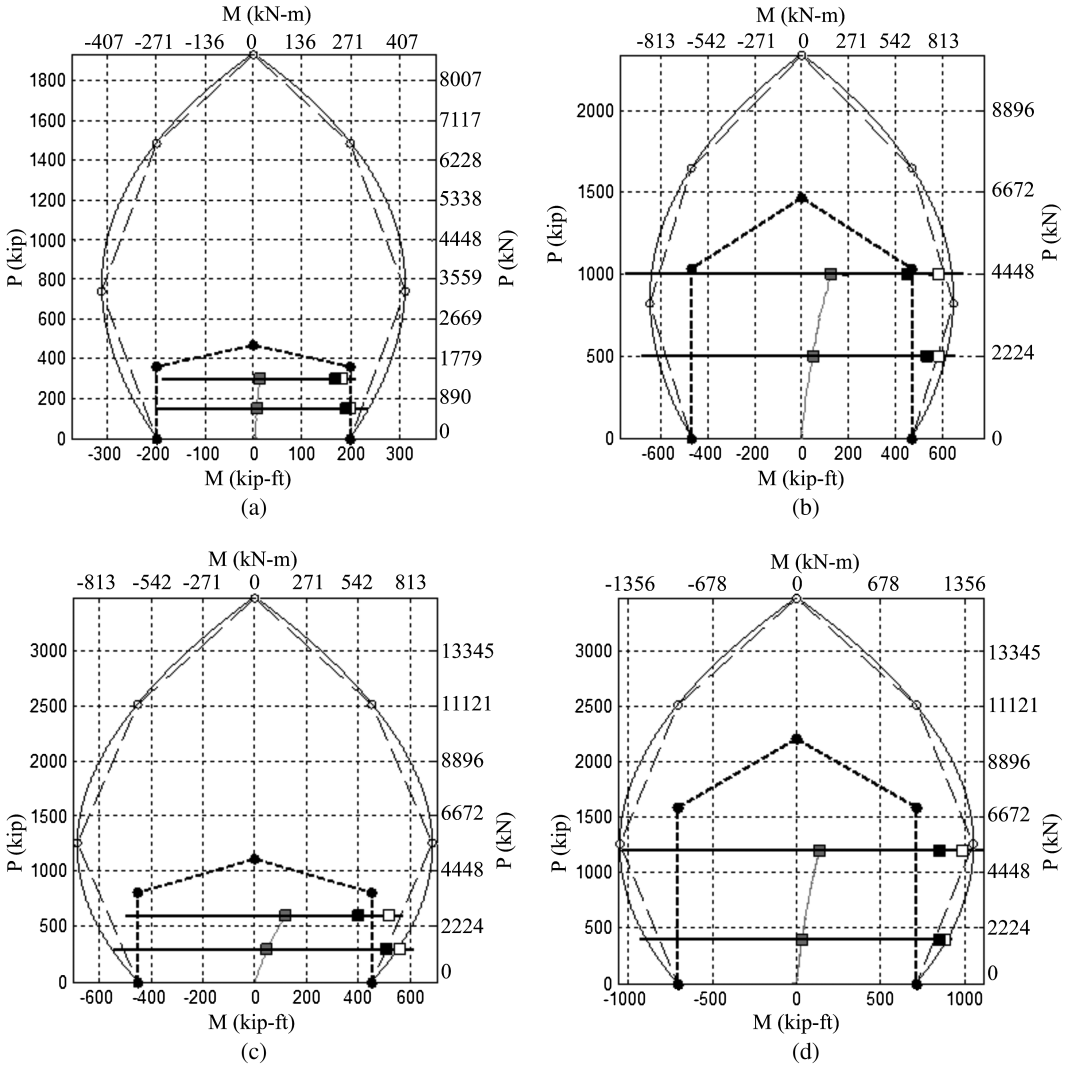

Fig. 6. $P-M$ interaction points extracted from tests in some CFT specimens under uniaxial loading LC2: (a) Specimen 6-C12-18-12; (b) Specimen 3-C20-18-5; (c) Specimen 8-Rw-18-12; (d) Specimen 9-Rs-18-12

aimed at probing the experimental $P-M$ interaction surface; results are presented in this paper and compared with the design equations from AISC (2010b). Further cycles of LC2 and LC3 load cases also enabled investigation of the cyclic response of CFT beam columns so that comparisons could be made to predictions from advanced computational models that follow strength and stiffness degradation exhibited during the tests.

During LC1, the specimens exhibited primarily elastic buckling, along with some inelastic buckling associated with minor material inelasticity (Perea 2010; Perea et al. 2013a); whereas some damage occurred during LC1, the instrumentation did not show any significant yielding, and thus additional assessment of interaction strength could be conducted in the specimens in the subsequent loading sequences. However, during LC2 and LC3, damage developed as steel local buckling and concrete crushing did accumulate at the column base, particularly for the stockier and rectangular specimens; such damage should be considered when utilizing these results. In the analyses carried out as part of this paper, the full loading history, including LC1, was simulated for the analyses that are compared to these experiments.

In load cases LC2 and LC3, the beam columns were under vertical force control with a constant compression load at varying levels and with horizontal displacement control following a prescribed displacement pattern. In most cases, the top rotations were under load control to hold to zero moment, so as to mimic a rotationally free boundary condition at the top in each coordinate direction. Twist was displacement controlled to zero so as not to induce spurious torsional displacements while investigating the axial and flexural strength of the specimens. However, torsional displacements were not expected to be high because all the specimens tested were doubly symmetric closed cross-sections that thus have high torsional stiffness. Because the base was fully fixed, the effective length factor in these cases was nominally $K = 2$. However, in a few cases that will be identified in the following discussion, the top rotations were under displacement control and held to zero rotation, thus having an effective length factor that was nominally $K = 1$.

For load case LC2, the specimens were subjected to uniaxial flexure, moving the top of the specimen along one horizontal axis. The loading for most specimens was along one of the main coordinate axes of the MAST loading system, which also aligned with the primary axes of the cross-section for rectangular specimens; however, for several of the circular specimens, the loading was along a diagonal coincident with the maximum initial imperfection in the beam column, as noted under the column labeled *Direction* on Table 2. For load case LC3, the specimens were subjected to biaxial bending, moving the top of the column in patterns spanning both horizontal

Table 3. Summary of Extracted $P - M$ Interaction Points from Uniaxial Flexural Loading (LC2)

Specimen	λ	LC	P (kN)	P/P_n	M_{total} (kN-m)	M_{net} (kN-m)	M_{AISC} (kN-m)	M_{tot}/M_{AISC}	M_{net}/M_{AISC}
2C12-18-5	1.55	2a	1,334.5	0.76	174.0	141.1	142.5	1.22	0.99
		2b	889.6	0.51	206.5	184.8	248.5	0.83	0.74
6C12-18-12	1.89	2a	1,334.5	0.63	246.5	227.8	268.2	0.92	0.85
		2b	667.2	0.32	268.3	257.6	268.2	1.00	0.96
10C12-26-5	2.38	2a	889.6	0.97	59.5	30.4	60.3	0.99	0.50
		2b	444.8	0.48	217.6	191.3	255.3	0.85	0.75
14C12-26-12	2.69	2a	444.8	0.45	214.9	209.1	298.1	0.72	0.70
		2b	889.6	0.91	140.1	122.7	140.5	1.00	0.87
3C20-18-5	1.06	2a	4,448.2	0.68	789.0	614.7	635.5	1.24	0.97
		2b	2,224.1	0.34	791.7	725.5	635.5	1.25	1.14
7C20-18-12	1.30	2a	4,448.2	0.46	1,027.6	860.8	676.4	1.52	1.27
		2b	2,224.1	0.23	907.0	849.7	676.4	1.34	1.26
11C20-26-5	1.62	2a	2,668.9	0.61	687.7	453.8	611.5	1.12	0.74
		2b	1,334.5	0.30	677.1	603.7	611.5	1.11	0.99
15C20-26-12	1.78	2a	3,558.6	0.74	614.2	420.7	603.3	1.02	0.70
		2b	1,779.3	0.37	619.9	538.9	603.3	1.03	0.89
4Rw-18-5	1.38	2a	2,668.9	0.64	759.5	637.9	453.1	1.68	1.41
		2b	1,334.5	0.32	795.5	745.7	591.1	1.35	1.26
8Rw-18-12	1.65	2a	2,668.9	0.54	700.1	536.8	610.4	1.15	0.88
		2b	1,334.5	0.27	755.9	689.6	610.4	1.24	1.13
12Rw-26-5	2.14	2a	1,779.3	0.80	350.8	328.0	326.2	1.08	1.01
		2b	889.6	0.40	594.5	575.8	663.5	0.90	0.87
16Rw-26-12	2.30	2a	889.6	0.38	644.1	630.5	632.1	1.02	1.00
		2b	1,779.3	0.75	290.7	265.2	502.7	0.58	0.53
5Rs-18-5	0.89	2a	4,448.2	0.67	1,123.7	1,112.7	640.8	1.75	1.74
		2b	2,224.1	0.33	1,108.9	1,105.9	898.8	1.23	1.23
9Rs-18-12	1.04	2a	5,337.9	0.54	1,342.7	1,156.6	962.9	1.39	1.20
		2b	5,337.9	0.54	1,342.7	1,156.6	962.9	1.39	1.20
13Rs-26-5	1.35	2a	1,779.3	0.33	1,151.4	1,113.9	966.6	1.19	1.15
		2b	3,558.6	0.67	691.3	610.0	816.2	0.85	0.75
17Rs-26-12	1.46	2a	1,779.3	0.30	1,133.2	1,041.8	988.3	1.15	1.05
		2b	3,558.6	0.60	794.0	540.8	988.3	0.80	0.55
Average								1.12	0.98
Standard deviation								0.27	0.27

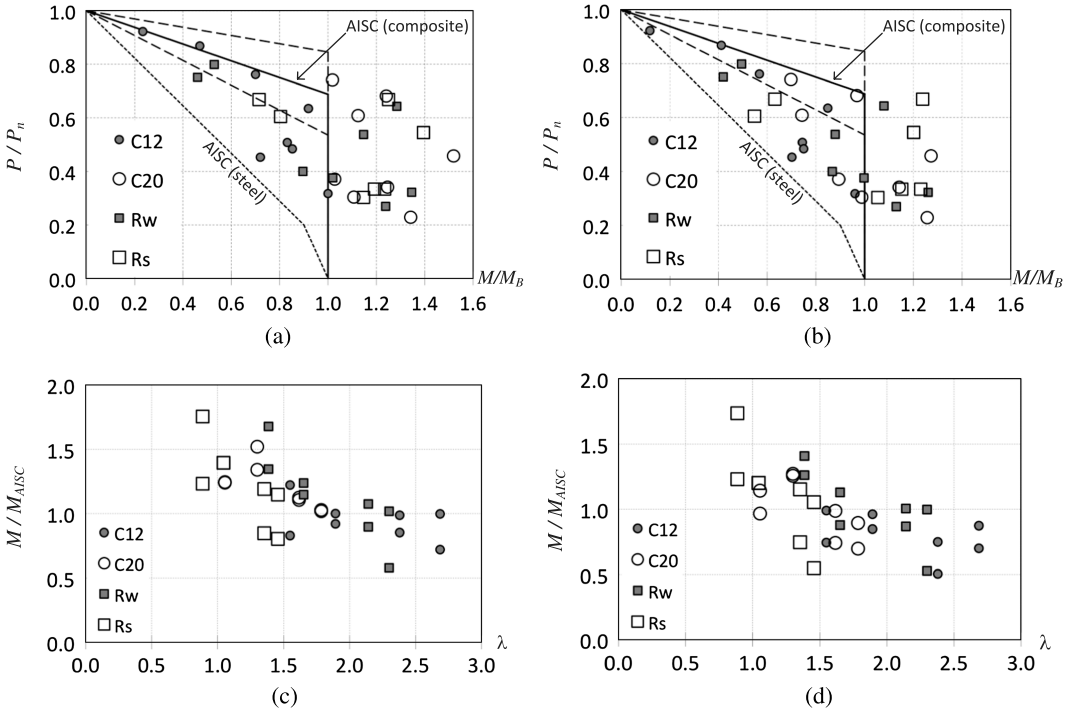

Fig. 7. Experimental total and net moments normalized to AISC (2010b) interaction strength: (a) total normalized interaction test points; (b) net normalized interaction test points; (c) total normalized moments versus slenderness; (d) net normalized moments versus slenderness

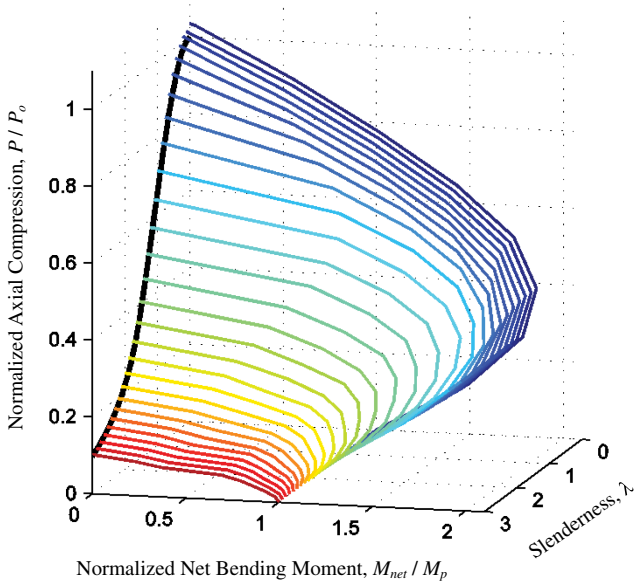

Fig. 8. Normalized $P-\lambda-M_{\text{net}}$ interaction diagram using a CCFT cross-section (HSS20 × 0.25 filled with a 83 MPa (12-ksi) concrete) obtained from nonlinear analyses (Denavit 2012)

axes. Several different displacement patterns or probes were used as illustrated in Fig. 4. Table 2, under the label *Reversal*, also summarizes the criteria used to initiate displacement reversals at the peak of a cycle: F_{max} refers to cases where displacements were reversed when the maximum lateral load was achieved; a percent value indicates that the reversal occurred at a predetermined interstory drift.

The displacements in the loading patterns were limited to either going just past the point of peak resistance to lateral loads or going to a preset desired level of drift. For Specimens 1 through 9, the target displacements in both LC2 and LC3 were defined by the peak lateral strength to lateral loads. In these cases, the drift was increased in displacement control until the peak strength to lateral loads, F_{max}, was obtained or when the tangent slope in the force-displacement response approached zero (indicating that the beam column was in an unstable configuration). For Specimens 10 through 18, predetermined loading patterns were used, typically with target displacements starting at ±1% drift and increasing by 1% drift in successive cycles up to the maximum stroke capacity of the MAST system (between 4 and 6% drift).

Combined Compression and Uniaxial Bending

The loading histories of LC2 allow the determination of the beam-column strength at each axial compression load level at which transverse displacement probes were conducted. Following the methodology described previously, incipient buckling is defined by the peak first-order moment (i.e., the peak lateral load times the member length). Typical moment-displacement results are shown in Fig. 5(a), including the components' first-order moment (M_1), $P\Delta$ moment, and the total second-order moment ($M_{\text{total}} = M_1 + P\Delta$). The extracted results are presented for some specimens in axial load–bending moment space in Fig. 6 as shown schematically in Fig. 5(b), with two quadrants shown as the results are sensitive to the initial direction of loading. The diagrams include:

- The cross-section P–M strength calculated using the plastic stress distribution method (thin dashed line passing through points $A-C-D-B$);
- The simplified $P-M$ interaction strength of the beam column using the theoretical effective length factor, K, and with reduction because of the stability effects as prescribed by the AISC commentary (AISC 2010b) (thick dashed line passing through points $A_\lambda - C_\lambda - B$); this simplified interaction curve is one of several options outlined in the AISC commentary;
- The $P-M$ path from the pure compression loading (LC1) up to the target axial load applied in LC2 (curved line from origin), and at the target axial loads, the moments generated by the initial imperfection (M_{imp});
- The horizontal $P-M$ paths from the uniaxial flexural loading cases (LC2);
- The total second-order moment at incipient buckling (M_{total}); and
- The net second-order moment ($M_{\text{net}} = M_{\text{total}} - M_{\text{imp}}$).

The test data for some specimens are presented in Fig. 6 in a format similar to Fig. 5(b) but showing both compression quadrants of the $P-M$ diagram. Because reversals of lateral loading take place just after passing the peak first-order moment, the second-order moment does not necessarily reach the cross-section strength. In other words, the ends of the moment paths at a given axial load (horizontal lines) do not necessarily achieve the cross-section $P-M$ (thin curve), and so they cannot be directly compared.

The extracted empirical interaction $P-M$ points for all the specimens are summarized in Table 3, and their normalized values are shown in Fig. 7. Fig. 7 shows the results normalized against design interaction diagrams proposed by AISC (2010b) for

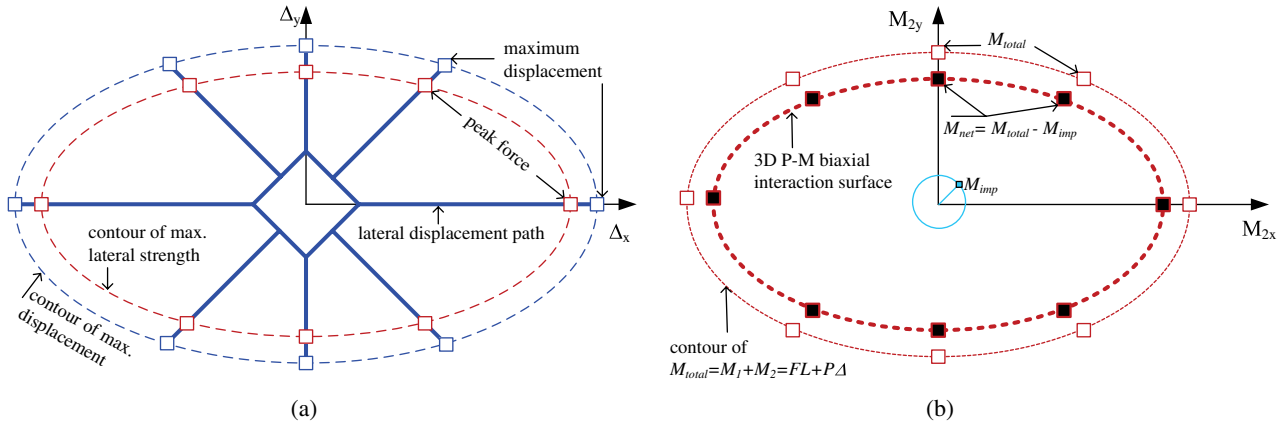

Fig. 9. Schematic illustration of the interaction surface from biaxial flexural and fixed axial loading (LC3): (a) bidirectional displacement path at the column top; (b) interaction surfaces with total and net moments at the column base

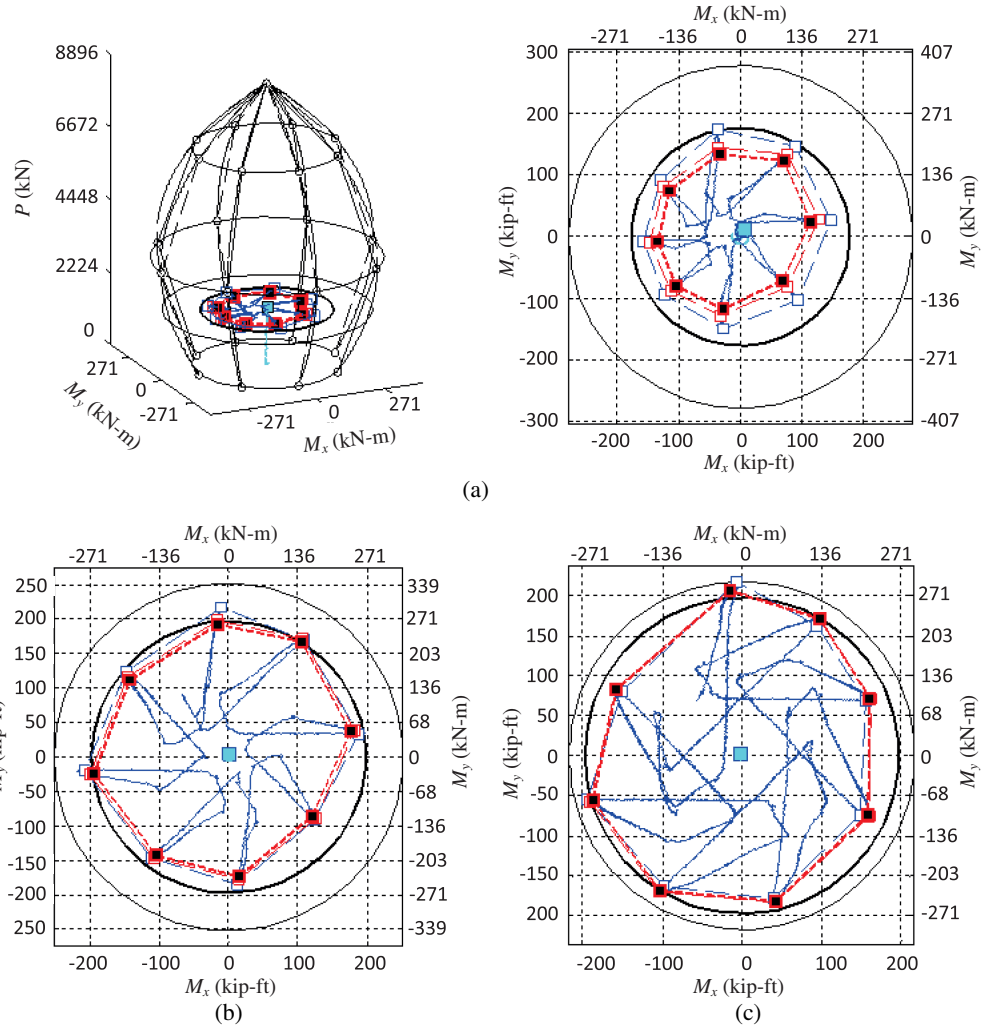

Fig. 10. Extraction of $P-M$ interaction points for Specimen 6-C12-18-12 from biaxial flexural and fixed axial loading (LC3): (a) $P = 1{,}668$ kN $= 375$ kip (left side in 3D, right side in 2D); (b) $P = 1{,}000$ kN (225 kip); (c) $P = 334$ kN (75 kip)

composite members. The target axial load is normalized by the nominal axial strength (P_n), and both the total and net second-order moments are normalized by the nominal flexural strength (M_B). Both P_n and M_B are calculated with the AISC specification (AISC 2010b). Because the normalized interaction point $C(P_{C\lambda}/P_n)$ depends on the contribution of the concrete in the composite section, which varies for each specimen, the upper and lower bounds for this point are shown as discontinuous lines in Figs. 7(a and b); as a reference, the normalized interaction diagram for steel members as defined by AISC (2010b) is also included in these figures as dotted lines. Figs. 7(c and d) show, respectively, how the normalized total and net moments vary with the slenderness parameter (λ). Based on these results, the following observations are highlighted:

- In general, the experimental net moments are close to the moment predicted by the AISC specification (AISC 2010b). Even with a considerable dispersion as noted in Fig. 7 and Table 3, the average ratio of the experimental moments over the AISC strength with stability reduction is 1.12 with the total moment ($M_{\text{total}}/M_{\text{AISC}}$) and 0.98 with the net moment ($M_{\text{net}}/M_{\text{AISC}}$); in both cases, the standard deviation is approximately 0.27.
- The differences between experimental results and design strengths can be accounted for by a number of factors, including: (1) the elastic analyses used in the design to obtain the required strengths are inherently different than the experimentally observed behavior because of the material nonlinearity that occurs in the experiments—the design interaction strength has been calibrated to the strengths that the elastic analysis would predict; (2) the simplicity of the design strength, in particular maintaining constant moment strength below the axial load P_C and ignoring the increased flexural strength near the balance point; (3) the net moments being based on the actual geometric imperfections of the specimen, not standardized imperfection values; and (4) the sequencing of the load cases and potential damage (i.e., steel local buckling and concrete crushing) that may have occurred in the specimen because of prior loading.
- A correlation is seen between the test-to-predicted ratios (either $M_{\text{tot}}/M_{\text{AISC}}$ or $M_{\text{net}}/M_{\text{AISC}}$) and member slenderness (λ). As shown in Figs. 7(c and d), most of the stockier specimens ($\lambda < 1.5$) achieve ratios larger than 1.0, whereas most of the more slender specimens ($\lambda > 1.5$) achieve ratios lower than 1.0. This behavior suggests a change in the shape of the interaction diagram with member slenderness that is not captured by the simplified interaction diagram outlined in the AISC commentary (AISC 2010b) of the specification. Similar results have been obtained from computational research (Denavit 2012). Fig. 8 shows the net axial–flexural–slenderness ($P-M_{\text{net}}-\lambda$) interaction obtained from fully nonlinear analyses of composite beam columns (Denavit 2012), from which constitutive materials and nonlinear elements were originally calibrated with the test data presented in

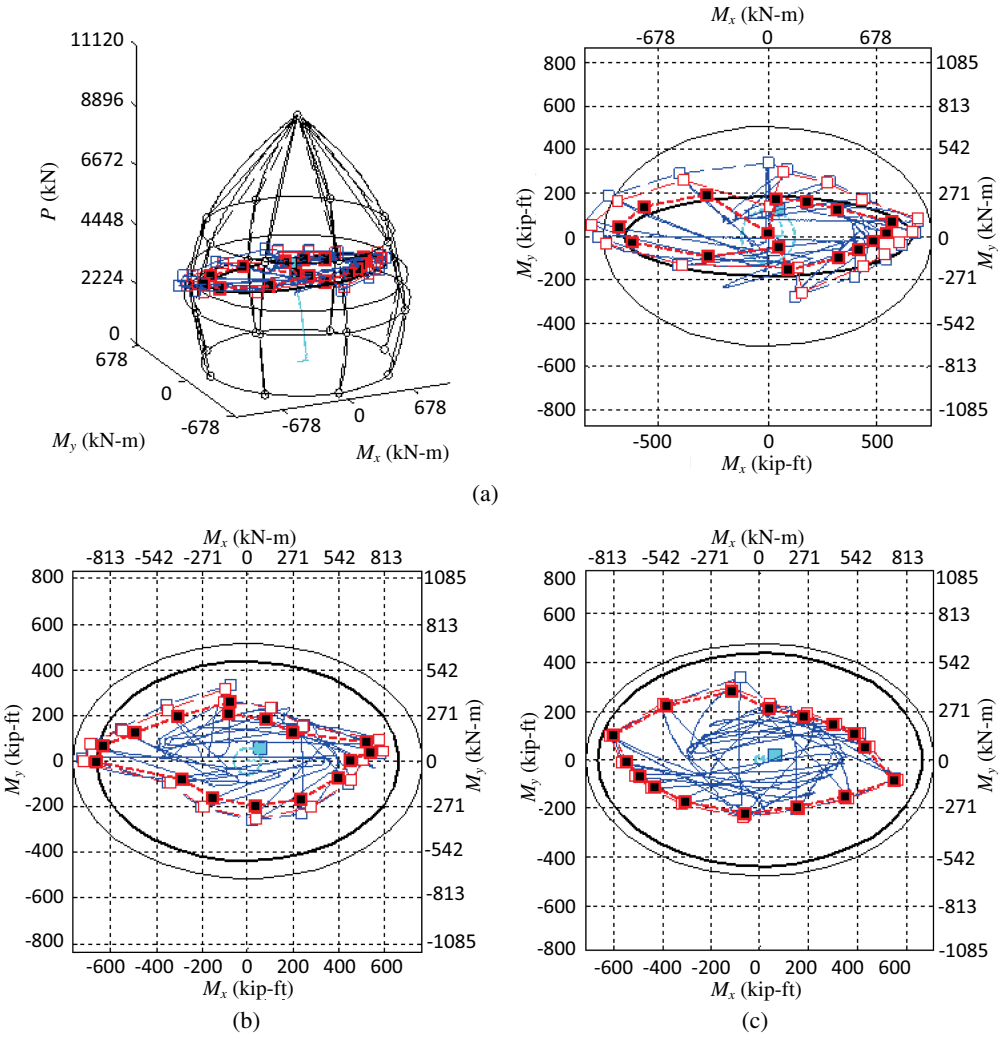

Fig. 11. Extraction of $P-M$ interaction points for Specimen 4-Rw-18-5 from biaxial flexural and fixed axial loading (LC3): (a) $P = 3{,}336$ kN $= 750$ kip (left side in 3D, right side in 2D); (b) $P = 2{,}002$ kN (450 kip); (c) $P = 667$ kN (150 kip)

this paper; the CCFT cross-section used in these analyses is an HSS20 × 0.250 ($F_y = 290$ MPa) filled with a 53-MPa concrete (same than the cross-section of the Specimens 7-C20-18-12 and 15-C20-26-12). These analyses illustrate how the $P-M$ interaction surface transitions from a full convex shape for stocky elements ($\lambda < 0.5$) to a more linear shape for slender elements ($\lambda > 1.5$).

Combined Compression and Biaxial Bending

The interaction strength limit points for the biaxial loading cases were extracted using the same methodology as for the uniaxial bending cases. The applied lateral displacement path of the column tip for Specimens 2 through 7 is shown schematically in Figs. 4(a) and 9(a). In these specimens, the displacement at the free end of the beam column was driven through different probes until the maximum flexural strength for each probe was reached. The contour of limit points found in each probe defines an interaction surface in displacement space [Fig. 9(a)]; the same limit points in moment space define the $M_x - M_y$ interaction surface at the applied axial load [Fig. 9(b)].

The complexity of the data obtained is shown in Figs. 10 and 11, in which a typical set of data for a constant axial load are shown in moment space. In these figures, a solid square near the center of the graph indicates the moment for LC1 at the axial force shown in the figure because of imperfections, and the circular path near the center of the graph shows the range of moments that may arise from this imperfection. Immediately outside this circle is the irregular path of biaxial flexure followed by the beam column during the displacement-controlled loading history; the hysteretic characteristics in these load histories are due to geometric imperfections in the direction of both the x- and y-coordinate axes. Inside this irregular path, a set of black and white squares extracted from the test data describes the envelope of net and total moments, respectively. Superimposed on these figures are circles [for circular concrete-filled steel tubes (CCFTs)] or ellipses [for rectangular concrete-filled steel tubes (RCFTs)] representing the AISC $M_x - M_y$ interaction strength for the beam column (thick solid lines) and the cross-section (thin solid lines). The shape of the interaction implied by the AISC specification is a diamond; the circles and ellipses were chosen to better represent the physical behavior.

Selected experimental results are shown in Figs. 10 and 11. There is a strong correlation between the experimental net moments and the AISC beam column nominal interaction surface for some specimens (e.g., Specimen 6-C12-18-12 in Fig. 10). However, a weaker correlation is seen for some specimens (e.g., Specimen 4-Rw-18-5 in Fig. 11). The worst correlation occurs in the weak axis of RCFTs; this poor correlation results as a consequence of the accumulation of damage because of local buckling and concrete crushing developed from previous load cases. The fact that most of

the specimens were close to the nominal strength envelope even after many probes at two or three different axial load levels is a testament to the robustness of these composite sections.

Conclusions

In this paper, the monotonic experimental response of slender circular and rectangular concrete-filled steel tubes was documented. For these experimental tests, the loading protocols were selected to obtain sets of axial–flexural strength ($P-M$) interaction points for both uniaxial and biaxial bending. The axial load levels used in the loading protocol were often applied between the anchor points C_λ and D_λ as defined by the AISC commentary (AISC 2010b), i.e., a zone in which the flexural strength in stockier members is typically larger than the flexural strength in pure bending. This paper investigates both the total flexural strength and the net moment that is achieved in CFTs for a given axial load level. The total flexural strength of the specimens for a given axial load level ($P-M_{\text{total}}$) extracted from the tests implicitly includes the reduction from the cross-section strength of the unusable flexural strength because of the instability effects from the axial compression. In contrast, the net strength for a given axial load ($P-M_{\text{net}}$) has an additional reduction of the unusable flexural strength that is caused by geometric imperfections in the member (e.g., out-of-straightness and out-of-plumbness), which were extensive in some of the slender members that were tested in this paper.

The net moments extracted from the test specimens of the stockier specimens typically exceeded the bilinear nominal interaction strength surface outlined in the AISC commentary (AISC 2010b), thus showing that this design approach underestimates the interaction strengths of the stockier specimens around the anchor point at D_λ by assuming that the interaction diagram extends directly from point C_λ to point B (i.e., the flexural strength in the presence of no axial force) as seen in the interaction diagrams in this work. The purpose of neglecting the additional flexural strength achieved in the presence of moderate axial compression is to provide a conservative estimate on the interaction strength, which was supported by the available experimental data at the time (Leon and Hajjar 2008; AISC 2010b). Future work could investigate how to engage this additional flexural strength for these stockier specimens.

The shape of the bilinear simplified diagram is less conservative in beam columns with intermediate slenderness; however, for very slender beam columns such as those tested in this paper, the AISC commentary interaction diagram is not conservative, as it is seen to overestimate the net flexural strengths for the test results in this work. The low net moment values are a consequence of the substantial flexural strength that is lost because of the initial large imperfections [in these tests, the imperfections were often larger than permissible tolerances allowed by ASTM A6/A6M (ASTM 2013) or AISC 2010a] and the accumulation of damage within the loading protocol. This unconservative behavior in slender beam columns suggests the need for a reexamination of the design equations for the calculation of interaction strength that serves both short and slender composite beam columns. It should be noted that the columns exhibiting unconservative predictions based on the current AISC specification occur at slenderness values that are generally well above what is commonly used in practice (i.e., $\lambda < 1.5$).

Experimental values of both the total and net moments under biaxial bending at constant levels of axial compression exhibit approximately circular interaction surfaces in CCFTs and elliptical interaction surfaces in RCFTs, as may be expected. However, as the loading protocol progressed in RCFTs, the interaction surfaces exhibited a reduction in size and changes in shape. This reduction is significant in RCFTs, particularly in the weak axis orientation, as a consequence of the progression of damage because of local buckling in the steel and loss of confinement in the concrete. Similar observations have been obtained in the computational studies (Denavit et al. 2010). These experimental results thus provide important characteristics to be achieved by advanced simulation models for CFT frame systems.

Notation

The following symbols are used in this paper:

E_c = concrete modulus of elasticity;
E_s = steel modulus of elasticity;
EI_{eff} = effective flexural stiffness of the composite section;
F = lateral force;
F_{max} = maximum lateral force observed during loading in a particular direction;
F_y = yield stress of the steel;
f_c = compressive strength of a concrete cylinder on the day of the test;
f_t = tensile strength of concrete;
f'_c = compressive strength of a 28-day concrete cylinder;
K = effective length factor;
L = member length;
M_{AISC} = member flexural strength calculated with the AISC specification;
M_B = flexural strength at the point B on the $P-M$ interaction diagram (equal to M_p);
M_C = flexural strength at the point C on the $P-M$ interaction diagram (equal to M_B);
M_{cs} = flexural strength of the cross-section at a given axial load;
M_D = flexural strength at the point D on the $P-M$ interaction diagram;
M_E = flexural strength at the point E on the $P-M$ interaction diagram;
M_{imp} = flexural strength consumed by imperfections when a given axial load is applied;
M_{net} = net flexural strength of the member ($M_{\text{net}} = M_{\text{total}} - M_{\text{imp}}$);
M_o = pure bending strength of the composite cross-section (equal to M_B);
M_p = plastic flexural strength (equal to M_B);
M_{total} = total flexural strength of the member at a given axial load;
M_{ufc} = unused flexural capacity ($M_{\text{ufc}} = M_{cs} - M_{\text{total}}$);
M_1 = first-order moment;
M_2 = second-order moment;
P = axial force;
P_A = compressive strength at the point A of the $P-M$ interaction diagram (also labeled as P_o);
$P_{A\lambda}$ = compressive strength at the point A_λ of the $P-M$ interaction diagram (equal to χP_A);
P_C = compressive strength at the point C of the $P-M$ interaction diagram (equal to $2P_D$);
$P_{C\lambda}$ = compressive strength at the point C_λ of the $P-M$ interaction diagram (equal to χP_C);
P_D = compressive strength at the point D of the $P-M$ interaction diagram (equal to $P_C/2$);
P_E = compressive strength at the point E of the $P-M$ interaction diagram;
P_e = Euler critical load;
P_n = member nominal compressive strength;

P_o = cross-section nominal compressive strength;
Δ = large or global deflections;
Δ_O = initial out of plumbness;
δ = small or local deflections;
δ_O = initial out of straightness;
λ = slenderness parameter; and
χ = slenderness reduction factor ($\chi = P_n/P_o$).

Acknowledgments

The work described in this paper is part of a NEESR project supported by the National Science Foundation under Grant No. CMMI-0619047, the American Institute of Steel Construction, the Georgia Institute of Technology, and the University of Illinois at Urbana-Champaign. In-kind funding was provided by Atlas Tube Inc. and LeJeune Steel Co. The valuable group effort of the MAST personnel in the experimental program is greatly appreciated. Any opinions, findings, and conclusions expressed in this material are those of the authors and do not necessarily reflect the views of the National Science Foundation or other sponsors.

References

American Concrete Institute (ACI). (2011). "Building code requirements for structural concrete and commentary." *ACI 318-11*, Farmington Hills, MI.

American Institute of Steel Construction (AISC). (2010a). "Code of standard practice for steel buildings and bridges." *AISC 303-10*, Chicago.

American Institute of Steel Construction (AISC). (2010b). "Specification for structural steel buildings." *ANSI/AISC 360-10*, Chicago.

ASTM. (2013). "Standard specification for general requirements for rolled structural steel bars, plates, shapes, and sheet piling." *ASTM A6/A6M-13*, West Conshohocken, PA.

Denavit, M. D. (2012). "Characterization of behavior of steel-concrete composite members and frames with applications for design." Ph.D. thesis, Dept. of Civil and Environmental Engineering, Univ. of Illinois at Urbana-Champaign, Urbana, IL.

Denavit, M. D., and Hajjar, J. F. (2010). "Nonlinear seismic analysis of CCFT members and frames." *Report No. NSEL-023, Newmark Structural Laboratory Report Series*, Dept. of Civil and Environmental Engineering, Univ. of Illinois at Urbana-Champaign, Urbana, IL.

Denavit, M. D., Hajjar, J. F., Perea, T., and Leon, R. T. (2010). "Cyclic evolution of damage and beam-column interaction strength of concrete-filled steel tube beam-columns." *Proc. of the 9th National Conf. on Earthquake Engineering*, E. M. Rathje and G. A. Atkinson, eds., Earthquake Engineering Research Institute, Oakland, CA.

Federal Emergency Management Agency (FEMA). (2009). "Quantification of building seismic performance factors." *FEMA P695*, Washington, DC.

French, C. W., et al. (2004). "Multi-axial subassemblage testing (MAST) system: Description and capabilities." *Paper No. 2146, 13WCEE*, Canadian Association for Earthquake Engineering, Ottawa, ON, Canada.

Gourley, B. C., Tort, C. T., Denavit, M. D., Schiller, P. H., and Hajjar, J. F. (2008). "A synopsis of studies of the monotonic and cyclic behavior of concrete-filled steel tube members, connections, and frames." Dept. of Civil and Environmental Engineering, Univ. of Illinois at Urbana-Champaign, Urbana, IL.

Hajjar, J. F., et al. (1997). "Effective length and notional load approaches for assessing frame stability: Implications for American steel design." *American Society of Civil Engineers Task Committee on Effective Length*, ASCE, New York.

Hajjar, J. F., et al. (2002). "A system for multi-axial subassemblage testing (MAST): initial developments." *Proc., ASCE Struct. Cong.*, Denver, CO, 313–314.

Hajjar, J. F. (2000). "Concrete-filled steel tube columns under earthquake loads." *Progr. Struct. Eng. Mater.*, 2(1), 72–81.

Kawaguchi, J., Morino, S., Shirai, J., and Tatsuta, E. (1998). "Database and structural characteristics of CFT beam-columns." *Proc. of the 5th Pacific Structural Steel Conf.*, Vol. 2, Pacific Council of Structural Steel Associations (PCSSA) and Korean Society of Steel Construction, Seoul, Korea, 955–960.

Leon, R. T., and Hajjar, J. F. (2008). "Limit state response of composite columns and beam-columns. Part II: Application of design provisions for the 2005 AISC specification." *AISC Eng. J.*, 45(1), 21–46.

Leon, R. T., Kim, D. K., and Hajjar, J. F. (2007). "Limit state response of composite columns and beam-columns. Part 1: Formulation of design provisions for the 2005 AISC specification." *AISC Eng. J.*, 44(4), 341–358.

Lundberg, J. E., and Galambos, T. V. (1996). "Load and resistance factor design of composite columns." *Struct. Safety*, 18(2–3), 169–177.

Nishiyama, I., et al. (2002). "Summary of research on concrete-filled structural tube column system carried out under the U.S.–Japan cooperative research program on composite and hybrid structures." *BRI Research*, Building Research Institute, Tsukuba, Japan.

Perea, T. (2010). "Analytical and experimental study on slender concrete-filled steel tube columns and beam-columns." Ph.D. thesis, School of Civil and Environmental Engineering, Georgia Institute of Technology, Atlanta.

Perea, T., Leon, R., Denavit, M., and Hajjar, J. (2010). "Experimental tests on cyclic beam-column interaction strength of concrete-filled steel tubes." *Proc. of the 9th National Conf. on Earthquake Engineering*, E. M. Rathje and G. A. Atkinson, eds., Earthquake Engineering Research Institute, Oakland, CA.

Perea, T., Leon, R., Hajjar, J., and Denavit, M. (2013a). "Full-scale tests of slender concrete-filled tubes: Axial behavior." *J. Struct. Eng.*, 10.1061/(ASCE)ST.1943-541X.0000784, Special Issue: NEES 1: Advances in Earthquake Engineering, 1249–1262.

Perea, T., Leon, R., Hajjar, J., and Denavit, M. (2013b). "Strategies for determining buckling loads of slender full-scale concrete-filled tube specimens." *Composite Construction in Steel and Concrete VII. International Conf. & Events (ICE)*, ASCE, Reston, VA.

Roik, K., and Bergmann, R. (1989). "Report on Eurocode 4: Composite Columns." *Rep. EC4/6/89*, Minister fur Raumordnung, Bauwesen und Stadtebau der Bundesrepublik Deutschland, Bochum, Germany.

Sakino, K., Nakahara, H., Morino, S., and Nishiyama, I. (2004). "Behavior of centrally loaded concrete-filled steel-tube short columns." *J. Struct. Eng.*, 10.1061/(ASCE)0733-9445(2004)130:2(180), 180–188.

Sulyok, M., and Galambos, T. V. (1995). "Reliability of composite columns and beam-columns in EC4." *Proc., Int. Coll. on Stability of Steel Structures*, Budapest, Hungary, 11257–11265.

Surovek-Maleck, A. E., and White, D. W. (2004). "Alternative approaches for elastic analysis and design of steel frames. I: Overview." *J. Struct. Eng.*, 10.1061/(ASCE)0733-9445(2004)130:8(1186), 1186–1196.

Tort, C., and Hajjar, J. F. (2003). "Damage assessment of concrete-filled steel tube members and frames." *Structural Engineering Rep. No. ST-03-1*, Dept. of Civil Engineering, Univ. of Minnesota, Minneapolis.

Varma, A. H. (2000). "Seismic behavior, analysis, and design of high strength square concrete filled steel tube (CFT) columns." Ph.D. thesis, School of Civil and Environmental Engineering, Lehigh Univ., Bethlehem, PA.